Atmospheric
Chemistry
and Physics
Discussions

Microphysical Properties of Frozen Particles Inferred from Global Precipitation Measurement (GPM) Microwave Imager (GMI) Polarimetric Measurements

Jie Gong[1,2], Dong L. Wu[2]

[1]Universities Space Research Association, Columbia, MD

[2]NASA Goddard Space Flight Center, Greenbelt, MD

Correspondence to: Jie Gong (Jie.Gong@nasa.gov)

Abstract. Scattering differences induced by frozen particle microphysical properties are investigated, using the vertically (V) and horizontally (H) polarized radiances from the Global Precipitation Measurement (GPM) Microwave Imager (GMI) 89 and 166 GHz channels. It is the first study on global frozen particle microphysical properties that uses the dual-frequency microwave polarimetric signals.

From the ice cloud scenes identified by the 183.3±3 GHz channel brightness temperature (TB), we find that the scatterings of frozen particles are highly polarized with V-H polarimetric differences (PD) being positive throughout the tropics and the winter hemisphere mid-latitude jet regions, including PDs from the GMI 89 and 166 GHz TBs, as well as the PD at 640 GHz from the ER-2 Compact Scanning Submillimeter-wave Imaging Radiometer (CoSSIR) during the TC4 campaign. Large polarization dominantly occurs mostly near convective outflow region (i.e., anvils or stratiform precipitation), while the polarization signal is small inside deep convective cores as well as at the remote cirrus region. Neglecting the polarimetric signal would result in as large as 30% error in ice water path retrievals. There is a universal "bell-curve" in the PD - TB relationship, where the PD amplitude peaks at ~ 10 K for all three channels in the tropics and increases slightly with latitude. Moreover, the 166 GHz PD tends to increase in the case where a melting layer is beneath the frozen particles aloft in the atmosphere, while 89 GHz PD is less sensitive than 166 GHz to the melting layer. This property creates a unique PD feature for the identification of the melting layer and stratiform rain with passive sensors.

Horizontally oriented non-spherical frozen particles are thought to produce the observed PD because of different ice scattering properties in the V and H polarizations. On the other hand, changes in the ice microphysical habitats or orientation due to turbulence mixing can also lead to a reduced PD in the deep convective cores. The current GMI polarimetric measurements themselves cannot fully disentangle the possible mechanisms.

1. Introduction

Cloud processes play an instrumental role in determining the surface precipitation characteristics (Rutledge and Hobbs, 1983; Gedzelman and Arnold, 1994; Igel et al., 2013; Tao et al., 2013). In particular, cloud ice processes are arguably among the most poorly understood, in part due to various ice crystal types and sizes, as well as multiple pathways in ice particle formation and evolution. While ice microphysical processes themselves cannot be readily observed from space, the integrated effects of these processes (e.g., cloud and precipitation structures, microphysical/macrophysical properties) can be inferred using remote sensing techniques.

It is imperative to distinguish between ice cloud and frozen precipitation in the atmosphere although they are both composed of various non-spherical particles (Wallace and Hobbs, 2006). Weather and climate models treat these hydrometeors quite differently by suspending ice clouds for a long duration but removing frozen precipitation unrealistically fast. The models account ice clouds in radiation calculations but often ignore the radiative fluxes and heating rates from frozen precipitation in the

air (Waliser et al., 2011). Hence, remote sensing of microphysical properties in frozen precipitation and their connection to ice clouds above and surface precipitation, like this work, will provide a valuable surrogate on climate models in representing cloud-precipitation processes.

Retrieving microphysical properties of frozen precipitation has been a challenge for spaceborne remote sensing. It depends not only on macrophysical variables (e.g., column integrated mass amount, particle size distribution, etc.), but also on frozen particle shape and orientation (Xie et al., 2015). Small pristine ice particles are observed with no preferred orientation when the ambient temperature is very cold, but become more horizontally oriented in warmer ice clouds (Noel and Chepfer, 2010). On the other hand, for large ice particles such as snow aggregates, it is often difficult to determine their orientation due to irregular shapes that are subject more to aerodynamic conditions than temperature (Xie, 2012).

Passive and active microwave techniques at high-frequencies (> 89 GHz) are proven to be quite valuable for ice cloud and snowfall remote sensing because of dominance of ice scattering, whereas low frequency microwave channels are more suitable for detecting liquid precipitation and water clouds (Skofronick-Jackson and Wang, 2000; Wu and Jiang, 2004). To infer the particle shape and orientation properties, polarimetric measurements are needed and have been explored in a number of earlier studies. For example, Czekala [1998] pointed out the possibility of using off-nadir paired polarized channels at 200-340 GHz to measure horizontally oriented ice crystals. Recently, Miao et al. [2003], Xie and Miao [2011] and Xie et al. [2012] applied a radiative transfer model to ground-based measurements, and found up to -10K polarization differences between the vertically (V) and horizontally (H) polarimetric (V-pol and H-pol, hereafter) observations at 150 GHz during snowfall events. For spaceborne remote sensing, Prigent et al. [2001; 2005] analyzed the polarimetric observations at 37 and 85 GHz from SSMI/S (Special Sensor Microwave Imager Sounder) and 85 GHz from TRMM-TMI (Tropical Rainfall Measurement Mission Microwave Imager), where they attributed significant polarimetric differences to horizontally oriented non-spherical liquid or frozen precipitating particles (Prigent et al., 2001; 2005). Studies using ground-based radar also suggested similar polarimetric difference distribution (e.g., Homeyer and Kumjian, 2015). Davis et al. (2005) studied the 122 GHz polarimetric radiances at a very large oblique view angle and found significant differences between V- and H-pol measurements, supporting the global presence of horizontally-aligned ice particles in the upper troposphere. In a further study with Monte-Carlo simulations, Davis et al. (2007) showed such a polarimetric difference remains detectable at 190-664 GHz from large oblique angles. In addition to the microwave techniques, lidar polarimetry at visible channels has also been used to infer ice particle orientation (e.g., Hu, 2007; Noel and Chepfer, 2010; Zhou et al., 2012, 2013), but limited to the top layer of ice clouds due to poor cloud penetration with lidar techniques. Microwave polarimetric observations at 90-200 GHz are capable of penetrating thick clouds, and yet very much under-utilized. With careful consideration of surface or liquid cloud effects, these polarimetric measurements can provide useful information on the shape and orientation of frozen particles in the atmosphere.

The launch of Global Precipitation Measurement (GPM) core satellite in February 2014 enables new investigations on microphysical properties of frozen ice particles and their connection to surface precipitation. Conically polarimetric scanning at high microwave frequencies (89 and 166 GHz) from GPM's Microwave Imager (GMI) enhances sensitivity to frozen precipitation particle scattering and preserves the polarimetric information from ice clouds. Combining with GMI radiances at low microwave frequencies and GPM radar reflectivity, simultaneous retrievals of frozen particle microphysical properties (e.g., bulk size and orientation parameters) can be achieved on a global basis.

In this paper we present an analysis of the global GMI's polarimetric measurements at 89 and 166 GHz to infer the microphysical properties of frozen particles above precipitating systems. In the analysis we also include the airborne 640 GHz polarimetric observations from the NASA's Compact Scanning Submillimeter-wave Imaging Radiometer (CoSSIR) instrument to extend the sensitivity to small ice crystals. Horizontally oriented non-spherical frozen particles, and the mixing induced by

Atmospheric
Chemistry
and Physics
Discussions

vertical motion are thought as the leading causes of the observed radiance polarimetric differences. Radiative transfer models (RTMs) are employed to further quantify these hypotheses.

This paper is organized to describe the data analysis technique and radiative transfer models in Section 2, followed by the GMI and CoSSIR observation results in Section 3. The working hypotheses on the observed polarized signals are discussed in

5   the subsequent section, with conclusions and future directions in the end.

2.   GMI data, analysis, and radiative transfer models

2.1   GMI polarimetric measurements

The GPM core satellite consists of a Dual-frequency Precipitation Radar (DPR) and a passive GMI instrument with 13 channels between 10 to 190 GHz, among which the 10.65, 18.7, 36.5, 89 and 166 GHz channels have V- and H-polarizations. In

10   this study, we use only the 89 and 166 GHz polarization data because at these high frequencies the scattering contributions from ice particles and frozen precipitation become significant. The GPM core satellite flies at an altitude of 407 km in a non-Sun-synchronized orbit, covering a latitude range of 68°S to 68°N. Its slow progressing rate over local time makes it feasible to study diurnal variability of cloud and precipitation. Its wider-than-TRMM latitude coverage now allows investigations of cloud/precipitation properties in the extra-tropics. GMI has a forward conical scan off-nadir at an angle of 48.5° (52.8° incidence

15   angle at the surface). GMI contains two sets of footprint sizes with different scan swaths. For low-frequency (LF) channels below and including 89 GHz, the scan swath is 885 km, but it becomes 835 km for high-frequency (HF) channels. Such a disparity in footprint size and swath requires a post-processing and regridding the raw radiance measurements (L1B) in order to intercompare the 89 and 166 GHz polarimetric measurements. Thus, we choose to use L1C-R product instead of L1B in our study. More details on comparing the 89 and 166 GHz datasets can be found in the Appendix A.

20   In this study we define the polarimetric radiance difference (PD) as $\Delta TB = TB_V - TB_H$. Fig. 1 shows a squall line event revealed in the GMI's dual-pol 89 and 166 GHz radiances and PDs on April 29, 2014. The squall line exhibits a clear centerline of deep convective cells and periphery of anvil clouds in the radiance maps (Fig. 1a and 1b), where brightness temperature (TB) is depressed strongly in both channels but their PDs are relatively small along the deep convective line. Away from this convective center line, PDs maximize in the anvil/stratiform precipitation region (on the order of 10 K) before diminish

25   gradually in the remote clear-sky/cirrus regions (0-5 K). This variation from convective cores to anvil outflow and further to clear sky is more obviously seen in the 166 GHz than 89 GHz maps, because of the increasing contribution of ice particle scattering at higher frequency microwave channels. It is also evident in Fig. 1c, where the 89 GHz PDs are more sensitive to polarimetric signals from ocean surfaces than the 166 GHz, exhibiting a large PD contrast between land and ocean. Such a land-ocean contrast is not readily seen in the TB maps.
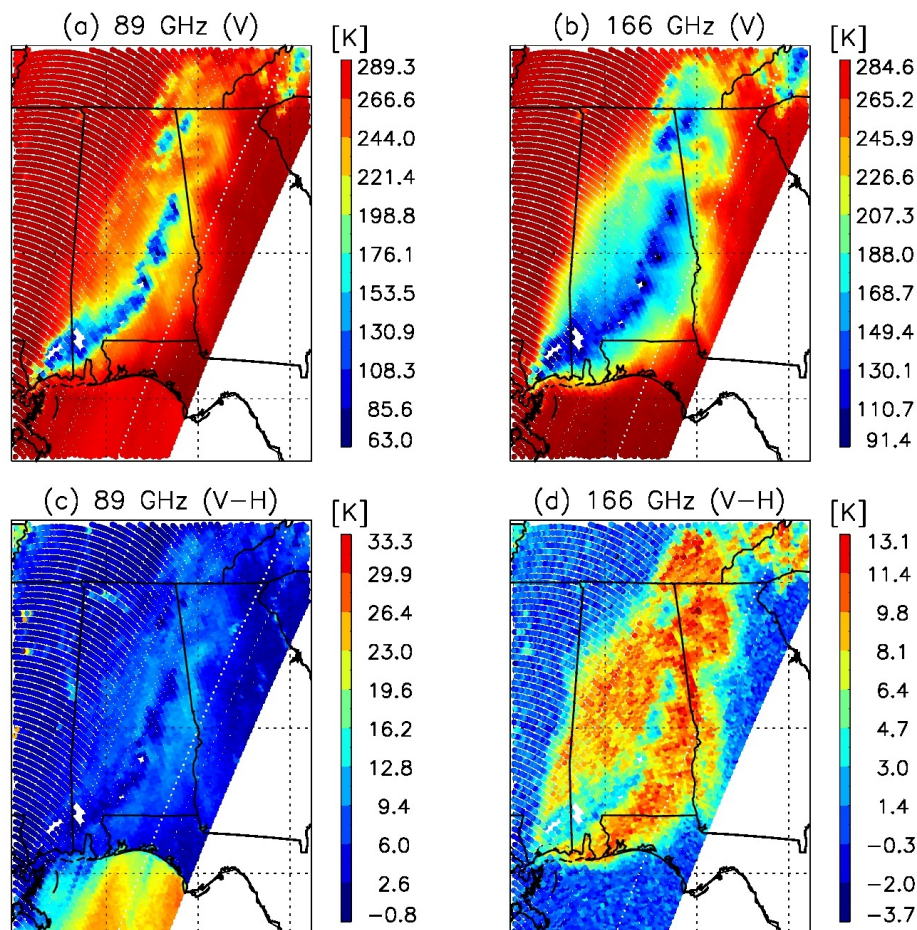
Figure 1: A squall line event on April 29, 2014 passing through the Southeast U.S. as observed with GMI 89 GHz (left panels) and 166 GHz (right panels) polarimetric channels. The GMI observed radiance distributions and polarimetric differences (PDs) are shown in the top and bottom, respectively.

5   Capable of penetrating clouds though, the PDs from 89 and 166 GHz contain surface polarization signals that need to be taken into account prior to cloud analyses. The polarized surface contributions are particularly strong over water where the degree of linear polarization (DoLP) of microwave radiances depends on surface roughness induced by wind and sea foams (Meissner and Wentz, 2012, Chen, 2014). As seen in Fig. 1c, the 89 GHz PDs exhibit a large contrast between land and ocean, but such a contrast disappears at 166 GHz. This feature is again manifested in Fig. 2, where observations over ocean, marked by

10   black open circles, spread to large PDs at the warmest end from 89 GHz observations, while this branch is not distinguishable at 166 GHz.

To study scattering properties of cloud and frozen particles jointly with the 89 and 166 GHz, we need to isolate cloud cases from the clear sky where the surface contributions are not negligible. To flag heavy cloudy cases, we use the simultaneous 183.3±3 GHz measurements, which show little sensitivity to surface emission due to the strong water vapor absorption but still with

15   enough sensitivity to deep convective clouds. As described in Gong and Wu (2013), a "3σ method" can be used to distinguish between clear- and cloudy-sky scenes for the Microwave Humidity Sounder (MHS) tropical observations. The "3σ method" first identifies the peak (TB_0) and standard deviation (σ) of the Probability Density Function (PDF) of a month-long radiance

Atmospheric
Chemistry
and Physics
Discussions

observation in a given region or a latitude belt, and then the cloudy-sky scene is defined at places where TB < TB_0 - 3σ. In this study, we apply the same methodology to select cloudy-sky scenes. Cloud occurring frequency after applying this "3σ method" is comparable to that observed by CloudSat radar (see Appendix D for a detailed map). Because of ocean/land differences, separate PDFs are computed for ocean and land surfaces in each 10° latitude bin. The three GMI channels (89, 166 and 183

5   GHz) have roughly the same (7.2 km × 4.4 km) footprint size, which minimizes the sampling error due to beam-filling effects between different frequencies. The combined sensitivities of the three channels will help to distinguish the scattering differences between frozen precipitation (large particles) and ice clouds (small ice crystals).

As a caveat, GMI swaths are mismatched between the LF and HF channels, offset by as much as 4 degrees in pointing (L1C, ATBD). Therefore, the L1C data are not appropriate for joint analyses of 89, 166 and 183 GHz measurements. Instead, we use

10   the L1C-R product that is derived from the L1B radiances using the nearest-neighborhood matching method to register collocated LF and HF observations. This re-registration procedure eliminates ~ 7% of the data, of which most occur at the edge of the LF scan swath. These missing data do not impact our climatological study. A comparison of the L1C-R and L1B datasets is given in the Appendix A.

While the 89 and 166 GHz polarimetric measurements are useful to infer microphysical properties of frozen precipitation, PD

15   at a higher frequency can reveal cloud properties with smaller ice crystals. To expand our study to ice clouds with small ice crystals (e.g., cirrus), we also include an analysis of the 640 GHz V- and H-pol data acquired by NASA airborne Compact Scanning Submillimeter-wave Imaging Radiometer (CoSSIR) during the Tropical Composition, Cloud and Climate Coupling (TC4) campaign in July-August 2007 (Evans et al., 2005; 2012). The CoSSIR instrument had a similar conical scan geometry to GMI in both forward and backward directions. About ~39000 CoSSIR conical samples from three TC4 flights are analyzed.

20   These samples were mostly over the Pacific Ocean near Central America and large enough to commensurate with the GMI statistics over the tropical oceans. We found that CoSSIR measurements were unreliable during the ascent/descent flight in altitude, and therefore only measurements at a cruise altitude above 19 km are used.

2.2   Data analysis

PD-TB_v relationship is a very useful diagnostic tool and will be used throughout this study. Fig. 2 shows a scatter plot of

25   PD vs. TB_v from the same squall line event reported in Fig. 1. As expected, for large oceanic PDs seen at 89 GHz, there is a distinct branch in Fig. 2a, showing a strong linear PD-TB_v relationship at the warm or clear-sky TBs. This branch is separated from the frozen particle scattering cluster that exhibits a bell curve in the PD-TB_v relationship. The bell curve is characterized by a peak of PD = ~10 K at TB_v = 220 K. Note that the surface branch is absent at 166 GHz due to strong water vapor absorption in the subtropics (Fig. 2b), but the bell curve is similar to the one at 89 GHz with peak of PD = ~10 K at TB_v = 190 K. The common

30   bell curve indicates that PD is small at the warmest (i.e., thin cloud or clear-sky) and coldest TB (i.e., deep convection) cases. As shown in the later sections, the bell curve appears to be universal at all latitudes.
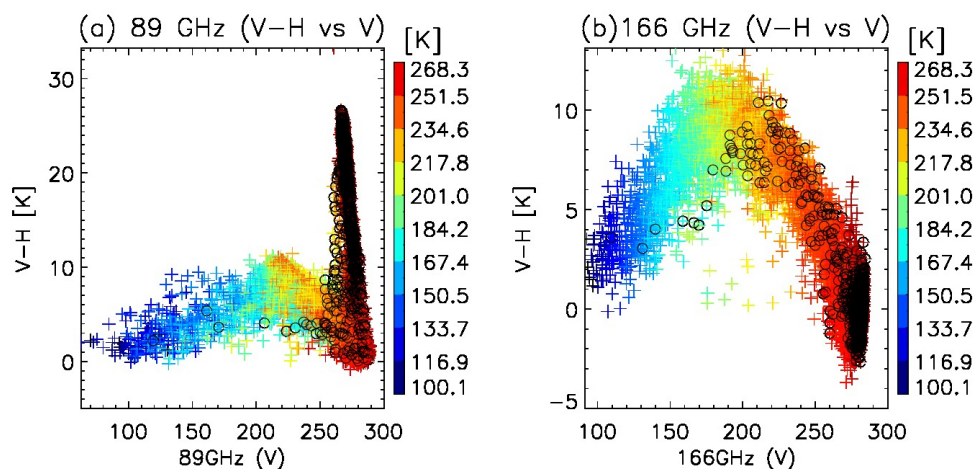
Atmospheric
Chemistry
and Physics
Discussions

Figure 2: The PD– TB_v scatter plots for the squall line case shown in Fig. 1 from 89 GHz (a) and 166 GHz (b). The points are color-coded by 183.3±3 GHz TB. Observations over ocean are further marked by black open circles.

The PDs observed from a conical scan are mostly positive in cloudy-sky scenes, because the cloud scattering tends to produce a larger TB depression due to horizontally-oriented non-spherical frozen particles. It is non-trivial to determine the magnitude of PD because other factors may play an important role as well. For example, as we can see from Fig. 1c, oceanic PDs are larger at 89 GHz because of higher V-pol emissivity on calm water surfaces than on windy surfaces, whereas land surfaces generally have little polarization. Figs.1-2 also show that the surface emissivity is frequency-dependent. In addition, liquid clouds and moisture layers may attenuate the PD signal from the surface (Greenwald et al., 1997). Negative PD values can be found in the GMI data as well but they are mostly in the clear-sky measurements and affected by noise. The probability density function (PDF) of negative PDs at 89 and 166 GHz behaves like a Gaussian distribution in most cases (Appendix B), from which we estimate the PD noise level to be ~ 0.5 K for 89 GHz and ~ 1 K for 166 GHz. It is interesting to observe that in some locations the negative PDs are non-Gaussian and have a significant number of measurements deviate from the Gaussian statistics. It is unclear what cause this statistical anomaly of the negative PDs, but it has been found in both 89 and 166 GHz data and the anomaly has an interesting geographical distribution. More details on the PD noise determination and the geographical distribution of the negative PDs can be found in Appendix B.

The PD climatology is computed globally and sorted according to latitude, TB_v, and PD value itself in 10°, 10K, and 1K bins, respectively. We also compiled a two-dimensional (2D) PDF with respect to PD and TB_v for each latitude bin. Monthly statistics of the PD - TB_v relationship are characterized by the peak and standard deviation of each 2D PDF. Only the cloudy-sky portion of the PD - TB_v relationship is reported in this study using the 3σ cloud detection with the 183.3±3 GHz radiances in each latitude band and computed separately for land and ocean.

Six months of GMI L1C-R data (June, July, and August in 2014 and 2015) have been compiled to study the cloudy-sky PD statistics. Although we use an earlier data version (V03) in this study, we find that the results are similar between V03 and V04 and choose to use the V03 data for the rest of paper. For the CoSSIR 640-GHz PD data, of which the campaign was based in Costa Rica, the statistics will be compared to the GMI data from the [0, 10°N] latitudinal bin.

To study the scattering properties of cloud ice and precipitation-sized frozen particles at 89 and 166 GHz, we make use of precipitation measurements from GPM DPR in our analysis. Galligani et al. [2013] found that large 85 GHz PDs of TRMM-TMI were often associated with a melting layer underneath (detected by TRMM-PR), suggesting a strong connection between cloud ice processes and surface precipitation. Thus, we employ the GPM Ku-band radar bright band (BB) flag to evaluate the 89 and

166 GHz PD properties and their connection to the presence of BB, as BB is always associated with stratiform precipitation. For this analysis, we first collocate the measurements between the Ku-band radar and the GMI 89 and 166 GHz data, and then tag the BB flag to each GMI measurement. The Ka-band radar also produces a product for classifying stratiform and non-stratiform precipitation cases, but the Ku radar BB flag is generally considered to be more reliable (Iguchi et al., 2010).

5   ## 2.3   Radiative Transfer Models (RTMs)

To evaluate impacts of frozen particle orientation and ice water content (IWC) on the TB and PD - TB_v relationship, two numerical RTMs are employed in this study. The first model, called RT4, is a variant of the Polarized Radiative Transfer Model Distribution (PolRadTran) developed by Evans and Stephens (1995). For our study, this model is configured to mimic GMI and CoSSIR's viewing geometry and channel frequencies, as well as to include several ice habitats (snowflake dendrites, hexagonal

10   plate, cylindrical columns, bullet-rosettes with 7 branches) and their scattering properties for diameter ranging from 20 to 2000 μm as described in Yang et al. [2013]. As described in Evans and Stephens (1995), the discrete dipole approximation (DDA) method is used to speed up the scattering calculation once the ice refractive index is provided. This index has weak dependence on temperature and we used the value at 240K in this study. Values at other temperatures (220K, 260K) have also been tested, and only show minor differences in the results. Frozen particle obey a Gamma size distribution, which is characterized by mean

15   mass-weighted equivalent sphere diameter (D_{me}). The desired gamma size distribution is achieved using an optimization procedure to adjust the equivalent volume diameter (D_e), where $D_{me} = \langle D_e^4 \rangle / \langle D_e^3 \rangle$. This optimization procedure assures that the truncated and discrete size distribution has the desired moments (i.e. D_{me} and dispersion width).

The RT4 simulations assume a uniform ice cloud layer with horizontally oriented non-spherical ice particles in a background atmosphere. Lambertian and Fresnel scatterings are used for land and ocean surfaces, respectively. Input variables are size

20   distribution (D_{me}), channel frequency, ice water path (IWP) and cloud layer bottom and top heights. Then, the model computes the V- and H-pol TB at the top of atmosphere (TOA) for a set of viewing angles, from which the GMI/CoSSIR TBs are derived by interpolating the model TB outputs to their viewing angles.

The RT4 model has several limitations. The modeled ice crystal shapes (except dendrites) represent primarily the pristine mid-latitude cirrus from synoptic outflows, which is not ideal for larger ice particles in the stratiform precipitating regions nor for

25   tropical deep convection cases. While the DDA calculation is very efficient for computing cirrus particle scattering, it is still computationally expensive for large particles, of which the valid range of IWP is limited to <1 kg/m^2 and D_{me} to <500 μm. Besides, the RT4 surface model and homogeneous ice cloud layers are often over-simplified compared to the reality. Because of these limitations, RT4 is perhaps mostly suitable for simulating the 640 GHz PDs where the surface contributes the least, compared to the lower frequency channels, and this channel is insensitive to precipitation-sized ice particles. Assuming randomly

30   particle orientation, Evans et al. [2012] applied the RT4 model with a dynamical mixture of different particle shapes to cloud ice retrievals on the CoSSIR data.

Another RTM for simulating frozen particle scattering, called Cloud Radiance Model (CRM), is based on the cloudy-sky forward model in Aura Microwave Limb Sounder (MLS) (Wu and Jiang, 2004; Gong and Wu, 2014). CRM is a non-polarized model, and it assumes only spherical ice particles in the scattering calculation. It has been applied to simulate cloud-induced

35   radiances at frequencies < 3 THz for a complicated viewing geometry (e.g., satellite nadir/limb sounding, in-cloud aircraft flight, and ground stations). Like RT4, CRM assumes the Gamma size distribution in the current study. Different from RT4, CRM allows the user to specify the vertical distribution of IWC or liquid water content (LWC) in the mixed-phase case, to study sensitivity of the cloud-induced radiance to cloud layer height. Cloud height is another free parameter in addition to particle size and IWP, which can alter the cloud radiance amplitude significantly in similar frequency range (Gong and Wu, 2014).

Atmospheric
Chemistry
and Physics
Discussions

Open Access

EGU

To study the effect of frozen particle orientation with CRM, we assume slightly different profiles of scattering volume coefficients at V- and H-pol, $\mathscr{E}_V(z)$ and $\mathscr{E}_H(z)$, respectively). The difference is characterized by the aspect ratio (AR) factor, defined as AR= $\mathscr{E}_H(z)/\mathscr{E}_V(z)$, which is assumed to be independent of height. In simulating the PD-TB relationship, we vary on the AR value but keep the rest model input parameters (e.g., D_{me}, IWC profile, etc.) unchanged. This is equivalent to the particle

5   AR effect in which horizontally-oriented particles tend to create a stronger scattering for the H-pol radiation than for the V-pol. Thus, we carry out two parallel simulations with different cloud scattering coefficients but identical settings for other parameters. We then associate the two simulations with the V- and H-pol cases to evaluate their differences or PD as would be observed by satellite/aircraft at a slant-viewing angle. Using this CRM approach, we will also be able to study the environmental effect on the expected PD as a function of water vapor attenuation in the atmosphere.

10   **3.   PD-TBv relationship observed by GMI and CoSSIR**

The bell-shape curve revealed in Fig. 2 is found to be universal for all latitude bins over land and ocean. Fig. 3 shows the tropical statistics over land and ocean for July 2014, where the PDF peaks from cloudy sky produce a similar PD bell curve for both land and ocean cases. The bell curve has a peak at $TB_V \sim 220$ K for 89 GHz and $TB_V \sim 200$ K for 166 GHz. Hence, despite the strong surface PD signal at 89 GHz the cloudy-sky PDs are quite similar between the two channels, both exhibiting a bell-curve with a

15   PD peak amplitude ~ 10K. Moreover, cloud-induced brightness temperature depression exhibits a similar dynamical range between 100-280 K at the two frequency channels, but the same ΔTB_V at 89 and 166 GHz features the scattering of frozen particles from different heights. Compared with 166 GHz, the 89 GHz TB_V has a narrower dynamic range (~ 60K) before reaching the PD peak for both oceanic and land conditions. This result is consistent with the TMI 85 GHz PD behavior reported by Prigent et al. [2005]. At 166 GHz, PD does not reach its peak until about 80 K colder than the clear-sky radiance. Besides, the

20   peak amplitude at 166 GHz is slightly larger than that at 89 GHz. The PD bell curve gradually diminishes at clear-sky scenes ($TB_V \sim 280$ K), but approaches ~ +2K at very thick convective clouds ($TB_V \sim 100$ K). These PD-TB_V features are also evident for synoptic scale clouds in the mid-latitude (see Fig. C1 or Fig. 4 for example).

The spatial distribution of cloud occurring frequency (CF) weighted PD (i.e., CF*averaged PD in each grid box) is high over active convective regions (not shown), similar to the CF from tropical deep convection zones and peaking near the equator in the

25   summer hemisphere. This distribution shows typical active convective centers (e.g., Central United States in July), as expected for thick anvil outflows from the deep convective cells. The PD-TB_v bell-curve is seen at latitude bins up to 50°N/S (Fig. 4 and Fig. C1).
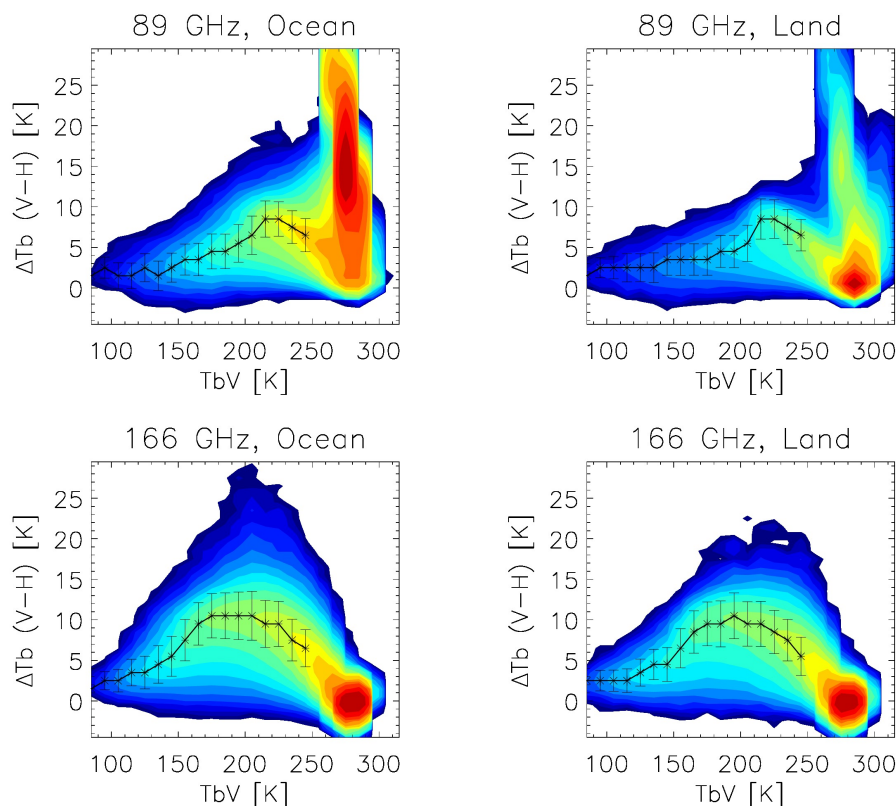
Atmospheric
Chemistry
and Physics
Discussions

Figure 3: Joint PDFs of ΔTB - TB_V statistics for the [0°, 10°N] latitude bin. The GMI 89 GHz (top) and 166 GHz (bottom) data in July 2014-2015 are used in the analysis, but separately for ocean (left) and land (right). Clear-sky data are excluded in computing the PDF peaks while the cloudy-sky PDF peaks are connected by black line with the standard deviation of PD shown for each bin. Cloudy-sky is determined by the "3σ threshold" method using the 183±3 GHz radiances. Color contour for the PDFs is in log scale.

Fig. 4 summarizes the latitudinal dependence of the bell-curves at each 20° latitude bin over land and ocean respectively. Six months of data (June, July and August of 2014 and 2015) are averaged together to increase the statistical robustness. The surface PD branch has been removed using the 183 GHz radiances and the "3σ threshold" separation for clear-cloudy skies. All the bell curves over ocean are essentially same, especially at 30°S-50°N. The wintertime high-latitude (70°S-50°S) belt is an exception. This is also evident at 89 and 166 GHz over land (Figs. 4c, d), which may be associated with the drier atmosphere at high-latitude in the winter atmosphere. Although the dynamic range of TB_V shrinks with increasing latitude, the PD peaks are still detectable and occur at about the same TB_V value (~220K) for the 89 GHz oceanic clouds credited to the large clear-sky variability and the resulting 3σ threshold. These findings suggest that the ensemble characteristics of the ice crystal shape and orientation that 89 GHz is sensitive to are consistent across all latitudes, which is a piece of good news to both the satellite retrieval and cloud modeling group, as many cloud microphysics assumptions during the retrieval and modeling processes are based on mid-latitude observations. The stringency of shape and orientation parameters ensures less uncertainty in the retrieving/modeling of the tropical and high-latitude atmosphere.

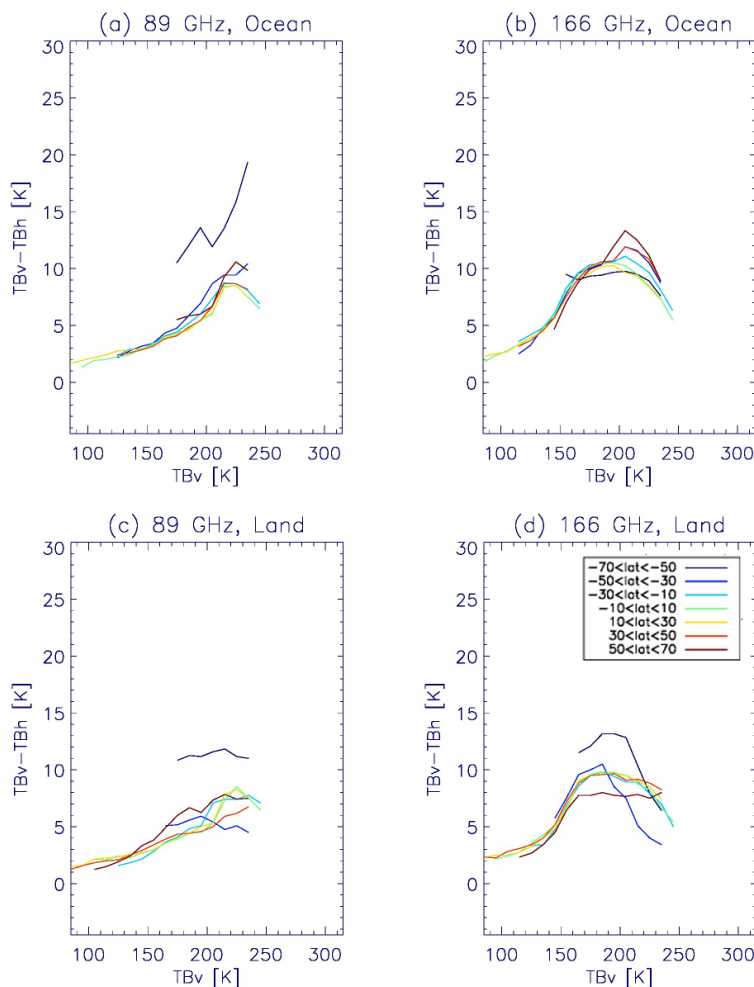Atmospheric
Chemistry
and Physics
Discussions

Figure 4: the PDF peak curves from different latitude belts (see label) derived from June-July-August 2014 and 2015 climatologies. Top panels for ocean and bottom panels for land conditions, respectively. Surface signal is removed using the 183.3±3 GHz radiance and the "3σ threshold" method.

5   The oceanic 166 GHz PDs at $TB_V = 200\text{-}220$ K appear to increase with latitude in both hemispheres (Fig. 4b). There is also a hint in Fig. 4a for 89 GHz although the tendency is rather weak. This latitudinal dependence of the PD amplitude could be due to latitude-dependent water vapor abundance, because ample water vapor can damp the PD signal. The water vapor damping is stronger in the tropics and consequently flattens the PD-TB curve more. The water vapor attenuation effect is also evident for ocean conditions at mid-high latitude of the winter atmosphere (30°S - 70°S), which is caused by the fact that the atmosphere

10   there is very dry and cannot block the surface signal anymore (e.g., Fig. C1d). However, the upper troposphere water vapor amount should be roughly symmetric between the two hemispheres (Solden and Lanzante, 1996), but the PD curves do not suggest such an inter-hemisphere symmetry. Over ocean, the PD peak amplitude is slightly larger in the summer hemisphere, while is contrary over land. Therefore, the role of water vapor in attenuating the PD is perhaps more complicated than expected. We will explore this in more detail in the next section.
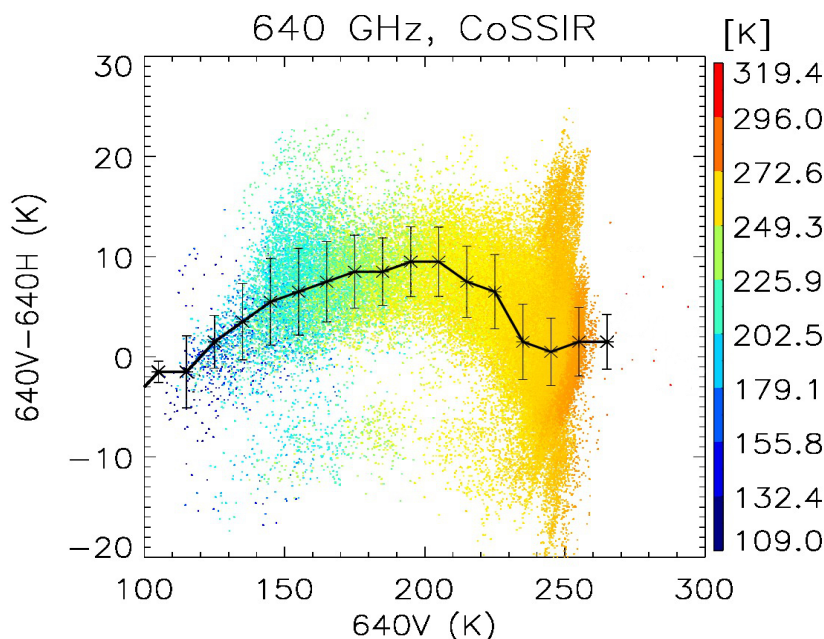
Figure 5: Scatter plot of quality-controlled CoSSIR PD - TB_V 640 GHz measurements from the TC4 campaign. Observations over land and ocean are not separated here. The black solid line with errorbars is the PDF peak, where bins beyond 260 K is excluded because of the sparseness of the data.

Studying the CoSSIR 640 GHz measurements from the TC4 campaign, we also find a bell curve in the PD-TB relationship (Fig. 5). Interestingly, the largest PD amplitude remains at ~ 10 K, and occurs at TB_V ~ 200 K. Some high PDs are found in thin cirrus cloud/clear-sky scenes near $TB_V = 250$ K and in optically thick cloud of $TB_V = 150$K, which are also associated with large negative PD values. These cases are found in the July 19th and August 6th flight legs but not in July 17th flight leg. Data qualities are considered much noisier in the former two flights than the latter one, but we still keep to show the original data from all three flight legs in Fig. 5 as the peak of PD-TB relationship alters little by including the noisier data (Frank Evans, personal communication).

To summarize, robust and significant PD signals from GMI's 89 and 166 GHz channels contain ample information about ice microphysics of frozen particles. There exists a universal bell-curve in the PD - TB relationships at all high-frequency microwave channels, including the 640 GHz observations from CoSSIR. They all show a peak amplitude of ~ 10 K at $TB_V =$ 200-220 K. What cause(s) the bell curve is an interesting question for remote sensing microphysical properties (size and shape) of frozen particles. In the next section, we will discuss two plausible mechanisms that may explain the observed features.

4. Discussions

4.1 A Simple Model for the PD-TB relationship

The leading hypothesis of the observed positive PD in cloudy sky is that the bulk ice properties produce different volume scattering coefficients in the V- and H-polarization. The bulk volume scattering coefficients can differ between the V- and H-polarization, depending on ice crystal shapes and their orientation. While the bulk scattering effects of cloud particles are detectable, details about how particles of various shapes organize themselves inside a cloud are beyond the capability of current

Atmospheric
Chemistry
and Physics
Discussions

remote sensing techniques. Clouds may produce little or no PD if the shaped particles are randomly oriented (e.g., tumbling in a turbulent environment). On the other hand, as discussed below, the PD tends to decrease with cloud optical thickness as a result of cloud self-extinction in the radiative transfer.

5   Let us assume that frozen particles are horizontally aligned, and the V- and H-pol extinction coefficients are dominated by scattering. Naturally V- and H-pol radiances pass through the same cloud with slightly different optical depths (τ_V and τ_H). We define the aspect ratio (AR) factor as $AR \equiv \tau_H/\tau_V$ to characterize this optical depth difference. Fig. 6 illustrates a simple two-layer model, where cloud optical depth is τ_2. Neglecting the water vapor attenuation, radiance at the top-of-atmosphere (TOA) can be expressed analytically as,

$$TB_V = T_{1V}e^{-\tau_{2V}} + T_I(1 - e^{-\tau_{2V}}) \tag{1}$$

10    $$TB_H = T_{1H}e^{-\tau_{2H}} + T_J(1 - e^{-\tau_{2H}}) \tag{2}$$

where T_J is the cloud source function, T_{1V} and T_{1H} are the polarized radiances from the background below the cloud resulted from the combination effect of surface, rain, or liquid cloud emissions. The cloud source function $T_J = \omega_0 \cdot T_{scat} + (1-\omega_0) \cdot T_2$ contains cloud emission $(1-\omega_0) \cdot T_2$ and scattering $\omega_0 \cdot T_{scat}$ contributions, where ω_0 is single scattering albedo. T_{scat} is the radiance scattered by clouds into the field of view, a result of the scattering phase function convolved with surrounding radiation, which is

15   approximately half of the upwelling radiation if the downwelling radiation is very small. The factor $(1 - e^{-\tau_2})$ takes into account the self-extinction process that is intrinsic to any source function in the radiative transfer. In the case that the background emission is unpolarized, i.e., $T_{1V} = T_{1H} = T_1$, then from Eqs. 1-2 we have

$$PD = TB_V - TB_H = (T_1 - T_J)(e^{-\tau_{2V}} - e^{-\tau_{2H}}) \tag{3}$$
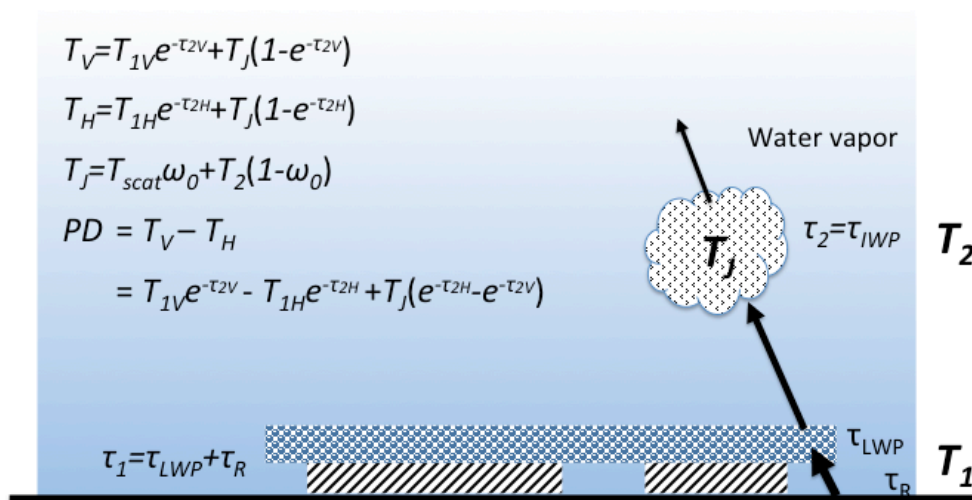
20

Figure 6: Schematic two-layer model with a liquid/rain/surface layer at T_1 and ice cloud layer at T_2 to explain the observed bell curve in the PD-TB relationship. See the text for more details and definition of the variables.

25

This simple 2-layer model (Eqn. 3) is able to reproduce several fundamental features of the observed PD-TB relationship. As shown in Fig.7a, it predicts the bell curve as seen in the GMI and CoSSIR polarimetric measurements, showing small PDs at

Atmospheric
Chemistry
and Physics
Discussions

Open Access

both small and large cloud optical depths or respectively warm and cold TBs. At large optical depths, as implied by Eqn. 3, the PD diminishes. At small optical depths, Eqn. 3 can be approximately written as

$$PD = (T_1 - T_J)(\tau_{2V} - \tau_{2H}) \qquad (4)$$

Because $T_J - T_I$ is roughly constant, this linear dependence on τ_{2V} - τ_{2H} helps to spread the slopes for different ARs because τ_{2V} - $\tau_{2H} = (1\text{-AR}) \, \tau_{2V}$.

The model can also explain the complex PD-TB relationships seen in the GMI oceanic data where the background surface emission is polarized. Because the 89-GHz channel is more sensitive to the polarized surface emission than the 166-GHz, the observed cloud PD often contains both surface and frozen particle contributions. As shown in Fig. 7b, the combined PD from the surface and cloud scattering can result in a tilted bell curve. The observed PD statistics in Fig. 3 are likely a mixture of the two cases shown in Fig. 7.

Finally, the conceptual model predicts weak dependence on channel frequency for the PD-TB relationship. The reason is as follows. If cloud extinction is dominated by scattering, τ is proportional to the 4th order of the frequency, i.e., $\tau = \alpha f^4$. Therefore AR is independent of frequency by definition. If the background emission is unpolarized (i.e., $T'_{1V} = T'_{1H} = T_1$), the PD from Eqns. 1-2 has a maximum of $(T_1 - T_2)(e^{-\tau_{2V}} - e^{-AR*\tau_{2V}})$ at $\tau_{2V} = \ln(AR)/(AR - 1)$, which is only weakly dependent on frequency. This weak-dependence of PD on frequency seems to be consistent with the observations that PD amplitudes barely increase from 89, 166 to 640 GHz.
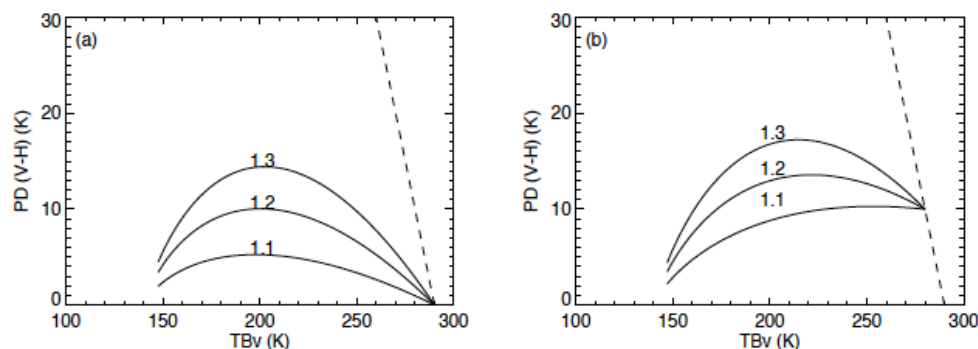

Fig.7. PD -T_B relationships from Eqns. 1-2 for different aspect ratios (ARs, value marked above each curve), assuming that the background emission is unpolarized (left, T'_{1V} - T'_{1H}=0) and polarized (right, T'_{1V} - T'_{1H}=10K). The dashed line indicates a typically polarized surface emission from wind-induced surface roughness.

Radiative transfer in this conceptual model is highly simplified. In order to test if this theory works in more realistic situations, we further test the AR values of 1.2, 1.3 and 1.4 using the non-polarized CRM. This model is detailed in Wu and Jiang (2004). To simulate polarized radiances, the CRM is run twice: one with the regular cloud extinction profile and one with the regular profile multiplied by AR. The two simulated radiances are differed to yield the PD as a function of AR. The surface temperature is set to 300 K in all simulations. The vertical distribution of IWC is assumed as a typical deep convective cloud profile with an anvil top (see Wu and Jiang, 2004 for a description), where the cloud bottom is 5 km (right above the freezing level in the tropics). Surface polarization is neglected in the simulations. A standard tropical atmosphere is used as the clear-sky background, and hence effects of the water vapor attenuation are included. Gamma distribution is used for ice particles with D_{me} = 200 µm. This large value takes into account a mixture of cloud and precipitation particles such that large TB depression can be produced. Other D_{me} values have also been tested. While the dynamic range of TB is sensitive to D_{me}, the peak PD amplitude is not. In the simulations only IWP is varied to create the PD-TB curves that best mimic the observations.
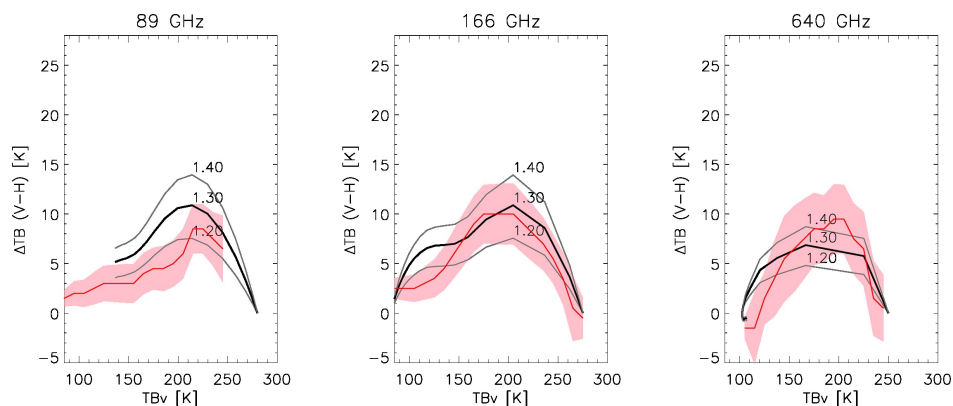
Figure 8: CRM simulated PD-TB curves in black for AR values of 1.2, 1.4 (thin) and 1.3 (bold), overlaid on top of the GMI and CoSSIR observations in red for (a) 89, (b) 166 and (c) 640 GHz with the standard deviation shown in pink shades. Surface contaminations are removed using the cloud flag derived from the 183.3±3 GHz channel.

Although AR in the range of [1.2, 1.4] produce a good envelope for the observed bell curves, AR = 1.3 seems to fit best overall to the observations. This AR value was also found in Davis et al. (2005) in studying the 122 GHz data. Having said that, there is an indication that the best fit of AR might increase with frequency, suggesting an increasing contribution of horizontally-oriented particles at higher frequencies. Since the higher frequencies are more sensitive to small frozen particles, it implies that small frozen particles have an increased percentage of the horizontal orientation. While it is difficult to infer the detailed composition of particle habits in these clouds, ice crystals in cirrus clouds (more sensitive by 640 GHz) are likely to have a predominant type (e.g., plate, column, etc.) and snow aggregates (more sensitive by 89 GHz) tend to have diverse irregular shapes. It is also found in the simulation that the modeled PD maximum decreases slightly at 640 GHz compared its value at 166 GHz, which is indicative of stronger water vapor attenuation at 640 GHz.

4.2 Full Polarized Model Simulation

AR is a parameter that characterizes the collective scattering property of frozen particle habitats. To study the relative importance of individual particle habitat, we use a fully polarized RT4, a variant of the PolTranRad model [Evans and Stephens, 1995], to simulate the PD-TB relationship. Four types of ice habitats and different D_{me} are used in the simulations, and the results are shown in Fig. 9 for 640 GHz assuming all frozen particles are horizontally aligned. As seen in Fig. 9, snowflake dendrites and cylindrical columns are most effective shapes to produce large PD values at 640 GHz, whereas cylindrical columns and bullet-rosettes can also induce a similar PD amplitude to what is measured by CoSSIR. The first two ice crystal types result in excessively large PDs in the PD-TB relationship. For bullet-rosettes, on the other hand, the PD does not produce the bell curve when the cloud becomes optically thick, whereas the cylindrical column shaped crystal with D_{me} between 200 and 300 µm produces the best agreement with the observation. According to Yang et al. [2013], this type of ice crystal with D_{me} = 250 µm, when projected to GMI's viewing direction, has an AR of 1.46, a value in a surprising good agreement with that from the CRM simulations shown in Fig. 8c. This consistency also supports the AR values used in the simple conceptual model and its radiative transfer argument for the bell-shape curve. We hope with more accurate multi-frequency polarimetric measurements that ice habitats may be retrievable from the PD - TB relationship eventually. More questions also rise up. For example, given that ice crystals have a vast variety of shapes in reality, why are the PD - TB relationship at 640 GHz similar to those at lower-frequency

Atmospheric
Chemistry
and Physics
Discussions

channels? Future field campaigns with polarimetric measurements from higher frequency channels should provide more insightful information to address similar questions.
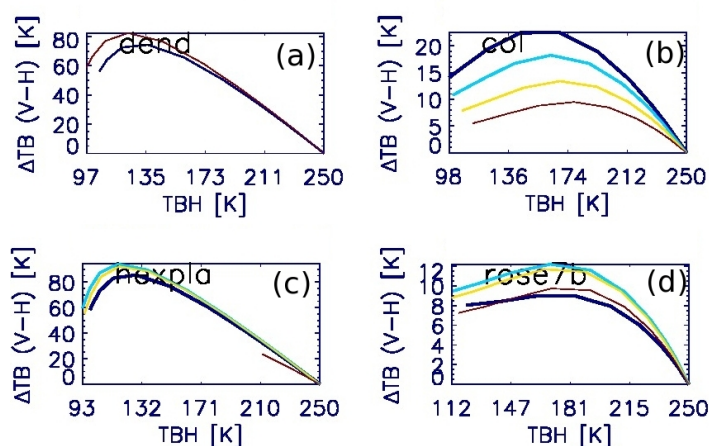
5   Figure 9: PolTranRad simulations of 640 GHz PD - TB relationship for four different ice habitats: (a) snowflake dendrite, (b) hexagonal plate, (c) cylindrical column, and (d) bullet-rosette with 7 branches. All frozen particles are assumed to be horizontally aligned. The red and blue in the snowflake dendrite simulation correspond to D_{me} = 200 and 300 μm, respectively. In the rest panels, red, yellow, cyan, and blue denote D_{me} = 200, 300, 400 and 500 μm, respectively.

     One of the top questions investigated in this study is: what process causes the low PDs of the bell curve at cold TBs? One

10   would argue that at cold TBs (i.e., strongly depressed by the scattering of deep convective clouds) the orientation of frozen particles were mostly random instead of horizontally aligned. As a result, those deep convective cold TB cases would yield a weaker PD. PolTranRad has another version called RT3, which allows to simulate effects from randomly orientated ice crystals, and the bell curve is found to be still present, despite the amplitude is rather small (< 3K) regardless of type of ice habitat used. Thus, the random orientation of frozen particles does not completely cancel out the particle shape effects, as revealed by the RT3

15   simulations.

     A varying mixture of randomly and horizontally-oriented particles may also provide a plausible explanation of the observed bell curve. If the larger mixing factor "α" corresponds to a more mixed environment inside clouds, α is likely to increase with deep convection strength, or a colder TB. On the other hand, horizontally aligned non-spherical particles are likely more effective to produce PDs in the anvil outflows than convective cores, because random orientation within the turbulent convective

20   core tends to cancel out the PD. This mechanism seems to have a support evidence in the ground-based Doppler radar observations (Homeyer and Kumjian, 2015), where they often found lower differential reflectivity (ZDR) near the deep convective core but larger values in the anvil outflows. In addition, the irregular shape of graupel found near convective cores likely contributes to a small PD as well as suggested in their paper.

4.3 PDs from melting layers and ice clouds

25   Since 89 and 166 GHz radiances are sensitive to scattering and emission of the precipitation-sized frozen particles, we need also to take into account the effects of the floating snow layer (Xie et al., 2012) or the melting layer close to the surface (Galligani et al., 2013) underneath the cloud layer. Although it is difficult to quantify the PD sensitivity separately for different layers of frozen particles, it is possible to evaluate the response of PD to the melting layer with the combined DPR-GMI

Atmospheric
Chemistry
and Physics
Discussions

observations. Melting layers manifest themselves as a unique bright band (BB) on the Ku-band radar reflectivity profile, as a result of stratiform rainfall. We therefore use the BB flag and precipitation flag in DPR's Ku-band radar Level-2 products to discriminate the stratiform and non-stratiform precipitation scenes. Non-stratiform precipitation types include convective rainfall and snowfall.
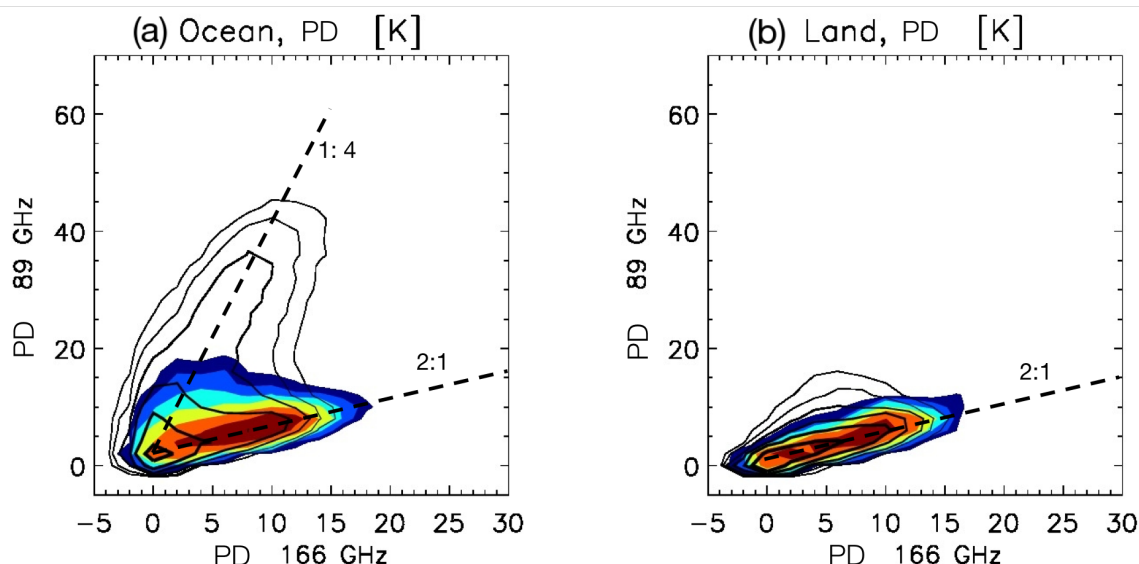

Figure 10: Joint PDF of 89 and 166 GHz PDs during January 2015 over (a) ocean and (b) land for precipitation with the bright band (color shaded) and without the bright band (black contours). Color and contours are in log scale.

Fig. 10a shows a joint 89 and 166 GHz PD PDF with rather diverse relationships for oceanic measurements with and without BB. There are two branches in the 89 and 166 GHz PD correlation characterized by different slopes: 1:2 and 4:1. The measurements in the 4:1 slope are dominated by the polarized ocean surface emission, whereas the 1:2 group has little contributions from the surface. Because the 1:2 branch over ocean is also associated with the strongly polarized ocean surface, it should be related to lightly precipitating scenes that otherwise would show much stronger PD signals. In the case with BB, most of the polarized surface emission is blocked by BB. For non-stratiform precipitation (without BB), most likely there will be no PD signal from both channels (i.e., the center of the black contours is near the origin point in Fig. 10a). This indicates that the dominant PD signals of 89 and 166 GHz indeed come from ice cloud for non-stratiform precipitation, even it is snowfall. When the melting layer is present, both 89 and 166 GHz PDs incline to be positive. As a result, when the melting layer is present, the peak of the joint PDF (dark red) moves to ~ 5K and 8K for 89 and 166 GHz, respectively, as shown by the color shades in Fig. 10a, implying that the melting layer in fact contributes partially to the PD signal. This finding is consistent with Galligani et al. (2013) where they found that 85 GHz PD of TRMM's TMI is likely positive when the melting layer is present. It is also consistent with the higher BB ZDR as observed by ground-based radars (e.g., Oue et al., 2014). While 166 GHz is more sensitive to smaller ice crystals than 89 GHz, the more positive PD response in the 166 GHz indicates that smaller ice crystals should be more obsolete and/or more horizontally oriented. Larger particles like snow aggregates likely exhibit irregular shapes and the scattering signal in 89 GHz would hence be less directional, resulting a smaller PD response in this channel. This finding is highly consistent with the weak increase of AR value with the increase of channel frequency in CRM simulations shown in Section 4.1. Moreover, frozen particles of all sizes tend to be more horizontally oriented for stratiform rainfall compared with non-stratiform precipitation.

Over land, the PD characteristics vary roughly the same way with that over ocean, but the 4:1 branch exhibited in the ocean case is not present in the land non-stratiform precipitation cases. The PDF peaks along the 1:2 line are different in the cases with and without BB. Other factors, e.g., liquid emission, may also play a non-trivial role here, but they are hard to be justified at this moment. Due to the complexity of melting layer, this paper does not intend to further quantify its role on the PD's

5   characteristics.

5. Conclusion and Future Work

High-frequency microwave polarimetric measurements contain ample information of frozen particle habitat and orientation. In this paper, the GMI 89 and 166 GHz PD characteristics are analyzed, which reveal a universal bell-curve in the PD - TB relationship. The bell curve also exists in the CoSSIR 640 GHz observations. All three frequency channels show a maximum PD

10   amplitude of ~ 10 K, occurring around TB = 200 – 220 K. Such a PD-TB relationship is robust for almost all frequencies and latitudes. Moreover, both 89 and 166 GHz channels show positive PD responses when a melting layer is present. This is a new feature not reported before, suggesting that at least part of the PD signals comes from the melting layer. The melting layer contribution is confirmed by comparing the PD statistics with non-stratiform precipitation situations.

Using a simple analytical radiative transfer model, we can explain the bell curve of the PD - TB relationship with the term of

15   aspect ratio (AR). In this simple model we assume that the V- and H-pol extinction coefficient profiles are similar and scaled by AR. According to this conceptual model, the PD is resulted from the stronger extinction at the H-pol but diminishes as the cloud scattering is too strong to become saturated to a constant TB in both polarizations. In addition, a fully polarized RTM is employed to study the effects of the frozen particle habitat and orientation on the PD. The mixing of different particle habitats and orientations inside deep convections break down the directional orientation, which cancels out the non-spherical shape

20   effect, which can result in a bell curve in the PD-TB relationship.

Since the fully polarized RTM simulation suggests a strong sensitivity of the PD's magnitude to ice habitat at 640 GHz, i.e., the shape factor, more observations from higher-frequency microwave or even IR channels would greatly facilitate the decode of the microphysical information of frozen particle shape and orientation at different portions of the crystal size spectrum.

Negative PD values are also found in these polarimetric measurements. The spatial distribution of the negative PDs does not

25   coincide with the most active convection regions. Although they have been hypothesized as a result of vertically-oriented frozen particles, careful consideration of measurement noise and surface properties is required before interpreted as a result of particle properties. The ample information embedded in PD sheds light on the future path of retrieval method development of more frozen particle microphysical properties.

Last but not the least, the observed PD-TB relationship has an important implication for cloud ice retrieval. Gong and Wu (2014)

30   used an empirical IWP - TB relationship derived from CloudSat-MHS (Microwave Humidity Sounder) measurements for the IWP retrieval. The observed PD in this study suggests a 30% IWP retrieval error if polarization is neglected.

Appendices

Appendix A: Mismatch and re-collocation of GMI low- and high-frequency channel measurements
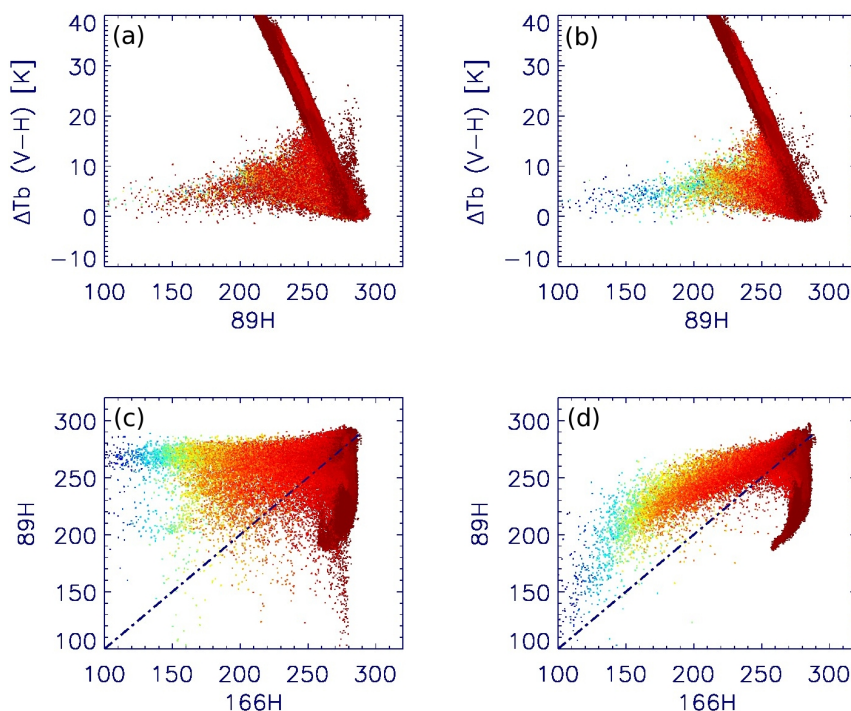

Figure A1: Scatter plots of 1-day tropical oceanic radiance measurements from L1B (a and c) and L1C-R (b and d) datasets, showing poorly (L1B) and correctly (L1C-R) georegistered radiance data. Points are color-coded by the 183.3±3 GHz radiance values with red being warm and blue being cold.

Fig. A1 illustrates the necessity of using L1C-R data to screen out the 89 and 166 GHz clear-sky scenes. Compared to L1B dataset that does not collocate the LF and HF channels, 183.3±3 GHz TB now corresponds much better with 89 GHz TB. Moreover, 166 and 89 GHz TB shows a much better coherence in the L1C-R data, showing two separate branches more clearly in Fig. A1 (d). The different slopes of these two branches correspond to the clear-sky and cloudy-sky characteristics, respectively, and the clear-sky branch also is the warmest in 183.3±3 GHz TB. Scatter behavior of Fig. A1(d) is very similar to comparable instrument, e.g., Special Sensor Microwave Imager and Sounder's 91 and 150 GHz channels (not shown).

Appendix B: Estimation of Instrument Noise and Distribution of Negative PD

GMI's 89 and 166 GHz PDs are not always positive. As a matter of fact, negative values occur frequently, and their occurrence is independent with TB. However, large negative PD only happens occasionally. The histogram of negative PD closely follows the Gaussian distribution, as shown in Fig. B1 by the black solid fitted lines. The "Gaussian_fit" function from IDL software package is used for this purpose, where the mean (μ) and standard deviation (σ) parameters are given as output. The standard deviation of the fitted Gaussian curve is a good estimate of the instrument noise (e.g., Wu et al. [2009]). Following the same analogy, we define the standard deviation parameter from the fitted Gaussian distribution as the GMI's instrument noise. σ is computed consequently for two months of 2015, January and July, for each 10° latitude belt, which varies limitedly

Atmospheric
Chemistry
and Physics
Discussions

among different latitudes, surface condition and season. The averaged σ is about 0.5 K for 89 GHz and 1 K for 166 GHz. Note that the radiance noise level should be derived by dividing σ by $\sqrt{2}$.

If the negative PDs are purely originated from instrument noise, they should be randomly distributed geographically. However, that is not the case for 166 GHz. If we plot out the occurrence frequency (OF) map of negative PDs that are smaller

5 than the negative instrument noise estimated using the aforementioned method, the OF is trivial at 89 GHz, indicating that negative PD is likely instrument noise. But for 166 GHz, large negative PDs occur quite frequently (up to 18% of the time), and they seem to favor the winter-hemisphere side of the tropical deep convections, as shown by Fig. B2. This is the first time such a geographical preference has ever been reported.

One theory explains the negative PD as the scattering effect from predominantly vertically oriented ice crystals that may be

10 oriented by the electromagnetic field created by lightning near the cloud top (Prigent et al., 2005; Homeyer and Kumjian, 2015). We can also consider the vertical orientation a counterpart solution of the horizontal orientation from the RTMs as the latter can only produce positive PD signals. However, global lightning distribution, which essentially connects to the tropical deep convective activities, correlates poorly with the geographic distribution of negative PDs (e.g., Cecil et al., 2014). Instrument noise is not likely the underlying cause for 166 GHz either since it would be randomly distributed otherwise. Having said that,

15 the secondary branch in the negative PD branch in Fig. 4 surely raised up more interests on studying the causes of negative PD. Although the actual cause remains unclear at this moment, negative PD, especially the large magnitude one, assures a rather attractive topic for future studies.
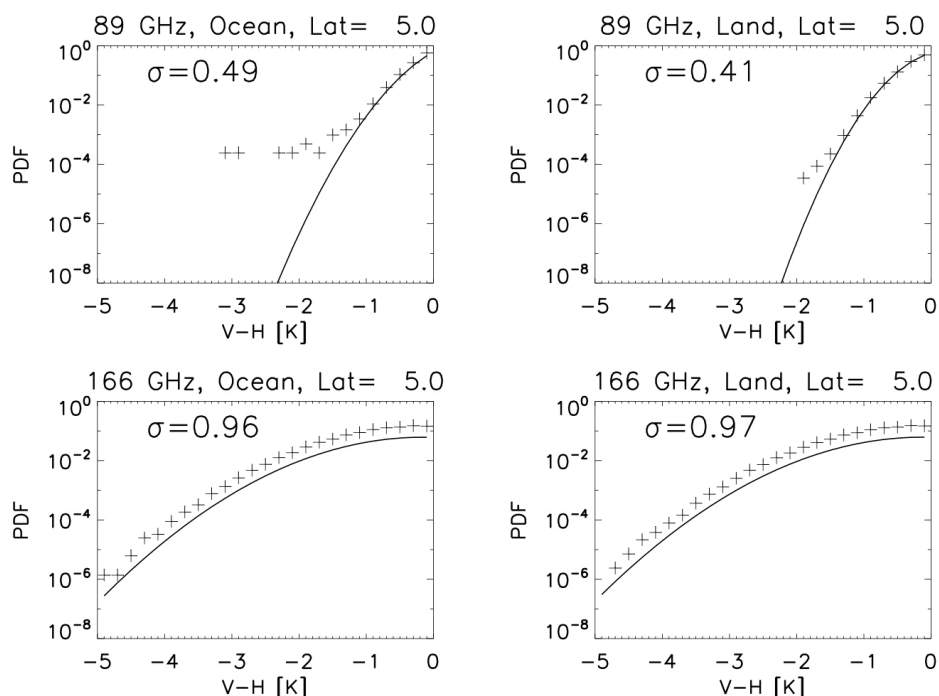
20

Figure B1: Histogram (cross) of negative PDs based on all GMI observations during January 2015 within the latitude belt of [0°, 10°]N for 89 (top) and 166 GHz (bottom) for ocean (left) and land (right) conditions. The Gaussian distribution fitted curve is plotted in black solid line, and the standard deviation from the fitted curve is marked on each plot.
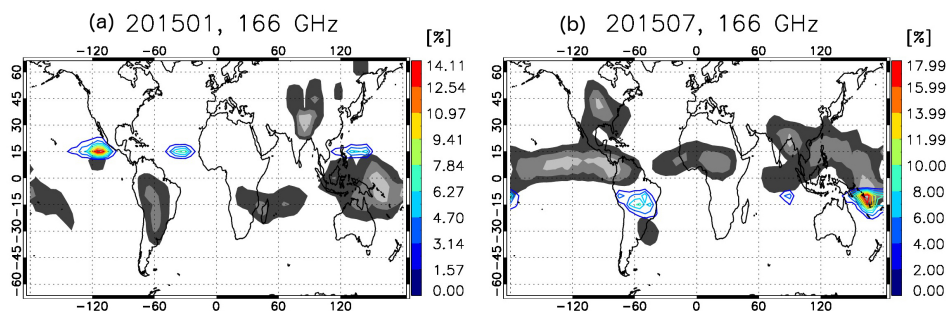

Figure B2: Geographical distribution (colored contours) of negative PD occurrence frequency during January (a) and July (b) 2015 for 166 GHz. Gray shades marked the occurrence frequency of $TB_v < 160$ K scenes, which is essentially equivalent to the occurrence frequency of deep convections, except that the signal over Tibet Plateau in Fig. B2(a) is probably induced by surface contamination.

Appendix C: PD – TB relationship at high latitudes

Fig. C1 shows the 2D PDF distribution from the same month climatology with Fig. 3, except that it is from another mid-latitude bin. Compared with Fig. 3, one can see very similar behavior of the PDF peak-connected lines. But the surface signal starts to emerge at 166 GHz at mid-latitude, as shown by the warm branch in the bottom panels of Fig. C1. "3σ threshold" method is proven here to be able to effectively exclude the surface signal in the PD – TB relationship, although it might be too stringent, especially for 166 GHz, as the clear-sky PD is only weakly dependent on the ocean surface roughness for this channel.
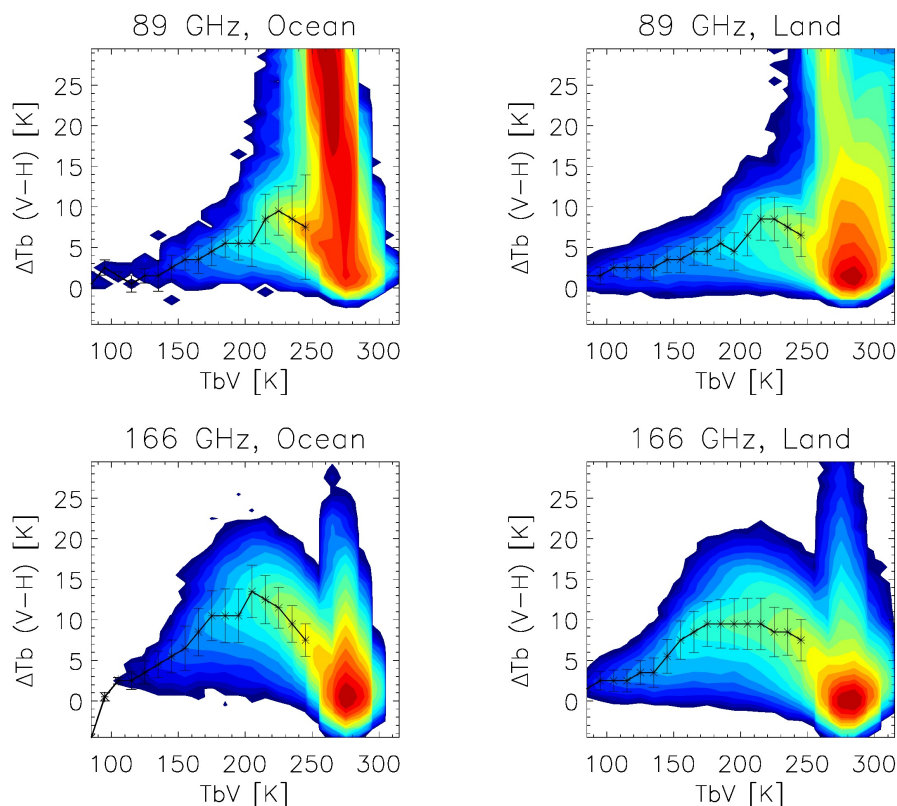
Atmospheric
Chemistry
and Physics
Discussions

Figure C1: Same with Fig.3, except for [45°, 55°N] latitudinal belt.

Appendix D: Cloud Occurring Frequency (CF) derived from the "3σ method"

To demonstrate the credibility of the "3σ method" on screening out the clear-sky scenes, we show the CF of July 2015 from the 89 and 166 GHz channels in Fig. D1. The geographic distribution of CF of anvil and deep convective clouds agrees well with that observed by the CloudSat radar (Sassen et al., 2009). Due to the stringent criteria set by the "3σ method", many cirrus scenes are classified as clear-sky scenes, and therefore cirrus cloud CF is obviously biased low using this method.
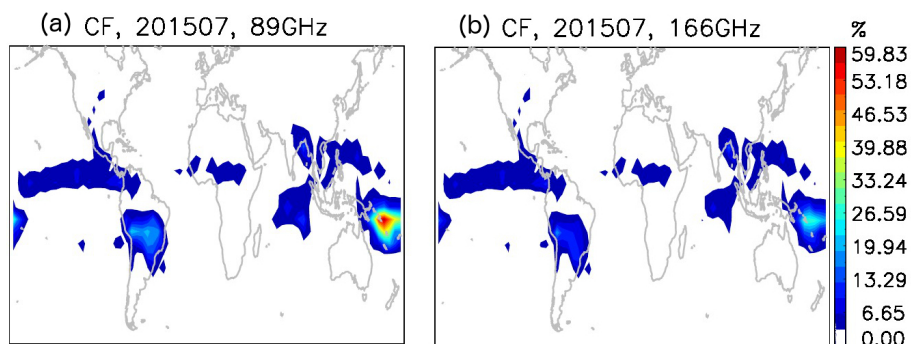
Atmospheric
Chemistry
and Physics
Discussions

Figure D1: Cloudy-sky cloud occurring frequency (CF) by applying the "3σ method" from GMI's 89 and 166 GHz observations during July 2015.

References

Cecil, D. J., D. E. Buechler, and R. J. Blakeslee (2014), Gridded lightning climatology from TRMM-LIS and OTD: Dataset description, *Atm. Res.*, **135-136**, 404-414.

Chen, X. (2014), Polarization signature in Micro-Wave Humidity Sounder Window Channels, Master Thesis, Florida State University.

Czekala, H. (1998), Effects of particle shape and orientation on polarized microwave radiation for off-nadir problems, Geophys. Res. Lett., 25, 1669–1672.

Davis, C. P., D. L. Wu, C. Emde, J. H. Jiang, R. E. Cofield, and R. S. Harwood (2005), Cirrus induced polarization in 122 GHz aura Microwave Limb Sounder radiances, *Geophys. Res. Lett.*, **32**, L14806, doi:10.1029/2005GL022681.

Davis, C. P., Evans, K. F., Buehler, S. A.,Wu, D. L., and Pumphrey, H. C. (2007), 3-D polarised simulations of space-borne passive mm/sub- mm midlatitude cirrus observations: a case study, Atmos. Chem. Phys., 7, 4149–4158, doi:10.5194/acp-7-4149-2007.

Evans, K. F., and G. L. Stephens (1995), Microwave radiative transfer through clouds composed of realistically shaped ice crystals. Part II: Remote Sensing of Ice Clouds, *J. Atmos. Sci.*, **52**, 2058-2072.

Evans, K. F., J.R. Wang, P.E. Racette, G. Heymsfield, L. Li (2005), Ice Cloud Retrievals and Analysis with Data from the Conical Scanning Submillimeter Imaging Radiometer and the Cloud Radar System during CRYSTAL-FACE, *J. Appl. Meter.*, 44, 839-859.

Evans, K. F., Wang, J. R., O'C Starr, D., Heymsfield, G., Li, L., Tian, L., Lawson, R. P., Heymsfield, A. J., and Bansemer, A (2012), Ice hydrometeor profile retrieval algorithm for high-frequency microwave radiometers: application to the CoSSIR instrument during TC4, *Atmos. Meas. Tech.*, 5, 2277-2306.

Galligani, V. S., C. Prigent, E. Defer, C. Jimenez, and P. Eriksson (2013), The impact of the melting layer on the passive microwave cloud scattering signal observed from satellites: A study using TRMM microwave passive and active measurements, *J. Geophys. Res. Atmos.,* **118**, 5667–5678.

Gedzelman, S. D. and R. Arnold (1994), The form of cyclonic precipitation and its thermal impact, *Mon. Weather Rev.*, **121**, 1957–1978.

Gong, J., and D. L. Wu (2013), View-angle-dependent AIRS cloudiness and radiance variance: Analysis and interpretation, *J. Geophys. Res. Atmos.*, **118 (5):** 2327-2339

Gong, J. and Wu, D. L. (2014), CloudSat-constrained cloud ice water path and cloud top height retrievals from MHS 157 and 183.3 GHz radiances, *Atmos. Meas. Tech.*, **7**, 1873-1890, doi:10.5194/amt-7-1873-2014.

Homeyer, C. R., & Kumjian, M. R. (2015), Microphysical characteristics of overshooting convection from polarimetric radar observations. *Journal of the Atmospheric Sciences*, **72(2)**, 870-891.

Hu, Y. (2007), Depolarization ratio–effective lidar ratio relation: Theoretical basis for space lidar cloud phase discrimination, Geophys. Res. Lett., 34, L11812, doi:10.1029/2007GL029584

Igel, A.L., S.C. van den Heever, C.M. Naud, S.M. Saleeby, and D.J. Posselt (2013), Sensitivity of warm frontal processes to cloud-nucleating aerosol concentrations. *J. Atmos. Sci.*, **70**, 1768-1783, doi:10.1175/JAS-D-12-0170.1.

Atmospheric
Chemistry
and Physics
Discussions

Open Access

EGU

Iguchi, T., S. Seto, R. Meneghini, N. Yoshida, J. Awaka, T. Kubota (2010), GPM/DPR Level-2 Algorithm Theoretical Basis Document.

Levizzani, V., Laviola, S., & Cattani, E. (2011), Detection and measurement of snowfall from space. *Remote Sensing*, *3*(1), 145-166.

5   Meissner, T., and Wentz, F. J. (2012), The emissivity of the ocean surface between 6 and 90 GHz over a large range of wind speeds and earth incidence angles. *Geoscience and Remote Sensing, IEEE Transactions on*, *50*(8), 3004-3026.

Miao, J., K.-P. Johnsen, S. Buehler, and A. Kokhanovsky (2003), The potential of polarization measurements from space at mm and sub-mm wavelengths for determining cirrus cloud parameters, Atmospheric Chemistry and Physics, 3, 39–48.

Precipitation Processing System (PPS), NASA GPM GMI Level 1B Algorithm Theoretical Basis Document (ATBD), NASA

10   Goddard Space Flight Center, November 2010.

Precipitation Processing System (PPS), NASA GPM GMI Level 1C Algorithm Theoretical Basis Document (ATBD), Version 1.4, NASA Goddard Space Flight Center, March 2015.

Noel, V., & Chepfer, H. (2010), A global view of horizontally oriented crystals in ice clouds from Cloud-Aerosol Lidar and Infrared Pathfinder Satellite Observation (CALIPSO). *Journal of Geophysical Research: Atmospheres*, *115*(D4).

15   Prigent, C., J. R. Pardo, M. I. Mishchenko, and W. B. Rossow (2001), Microwave polarized signatures generated within cloud systems: Special Sensor Microwave Imager (SSM/I) observations interpreted with radiative transfer simulations, *J. Geophys. Res.*, 106(D22), 28243–28258.

Prigent, C., E. Defer, J. R. Pardo, C. Pearl, W. B. Rossow, and J.-P. Pinty (2005), Relations of polarized scattering signatures observed by the TRMM Microwave Instrument with electrical processes in cloud systems, Geophys. Res. Lett., 32,

20   L04810,Skofronick-Jackson, G. M. and J. R. Wang (2000), The Estimation of Hydrometeor Profiles from Wideband Microwave Observations. *J. Appl. Meteor.*, **39**, 1645–1656.

Oue, M., T. Ohigashi, K. Tsuboki, and E. Nakakita (2015), Vertical distribution of precipitation particles in Baiu frontal stratiform intense rainfall around Okinawa Island, Japan, J. Geophys. Res. - Atmos., **120**, 5622–5637, doi:10.1002/2014JD022712.

25   Rutledge, S. A. and P. Hobbs (1983), The mesoscale and microscale structure and organization of clouds and precipitation in mid-latitude cyclones, 8, a model for the seeder-feeder process in warm-frontal rainbands, *J. Atmos. Sci.,* **40 (5)**, 1185 – 1206.

Sassen, K., Z. Wang, and D. Liu (2009), Cirrus clouds and deep convection in the tropics: Insights from CALIPSO and CloudSat, *J. Geophys. Res.*, **114**, D00H06, doi:10.1029/2009JD011916.

Soden, B. J., and J. R. Lanzante (1996), An assessment of satellite and radiosonde climatologies of upper-tropospheric water

30   vapor, *J. Clim.*, **9**, 1235 – 1250.

Tao, W.-K., J.A. Santanello, M. Chin, S. Zhou, Q. Tan, E.M. Kemp, and C.D. Peters-Lidard (2013), Effect of land cover on atmospheric processes and air quality over the continental United States – a NASA Unified WRF (NU-WRF) model study. *Atmos Chem. Phys.,* **13**, 6207-6626.

Wu, D. L., and J. H. Jiang (2004), EOS MLS Algorithm Theoretical Basis for Cloud Measurements, Technical Report, *Jet*

35   *Propulsion Laboratory,* D-19299/CL#04-2160, A TBD-MLS-06.

Wu, D. L., et al. (2009), Comparisons of global cloud ice from MLS, CloudSat, and correlative data sets, *J. Geophys. Res.*, **114**, D00A24, doi:10.1029/2008JD009946.

Wu, D. L., Lambert, A., Read, W. G., Eriksson, P., & Gong, J. (2014), MLS and CALIOP cloud ice measurements in the upper troposphere: A constraint from microwave on cloud microphysics. *Journal of Applied Meteorology and Climatology*, **53(1)**, 157-

40   165.

Xie, X., and J. Miao (2011), Polarization difference due to nonrandomly oriented ice particles at millimeter/submillimeter waveband, Journal of Quantitative Spectroscopy and Radiative Transfer, 112, 1090–1098.

Xie, X., U. Löhnert, S. Kneifel, and S. Crewell (2012), Snow particle orientation observed by ground-based microwave radiometry, Journal of Geophysical Research, 117, D02206, doi:10.1029/2011JD016369.

5   Xie, X., S. Crewell, U. Löhnert, C. Simmer, and J. Miao (2015), Polarization signatures and brightness temperatures caused by horizontally oriented snow particles at microwave bands: Effects of atmospheric absorption. *J. Geophys. Res. Atmos.*, 120, 6145–6160.

Yang, P., Lei Bi, Bryan A. Baum, Kuo-Nan Liou, George W. Kattawar, Michael I. Mishchenko, and Benjamin Cole (2013), Spectrally Consistent Scattering, Absorption, and Polarization Properties of Atmospheric Ice Crystals at Wavelengths from 0.2 to

10   100 μm. *J. Atmos. Sci.*, **70**, 330–347.

Zhou, C., Yang, P., Dessler, A. E., Hu, Y., & Baum, B. A. (2012), Study of horizontally oriented ice crystals with CALIPSO observations and comparison with Monte Carlo radiative transfer simulations. *Journal of Applied Meteorology and Climatology*, *51*(7), 1426-1439.

15